Engineering 18 (2022) 173–185

Contents lists available at ScienceDirect

Engineering

journal homepage: www.elsevier.com/locate/eng

Research
Green Chemical Engineering—Article

Dry Reforming of Ethane over FeNi/Al–Ce–O Catalysts: Composition-Induced Strong Metal–Support Interactions

Tao Zhang, Zhi-Cheng Liu, Ying-Chun Ye, Yu Wang, He-Qin Yang, Huan-Xin Gao, Wei-Min Yang *

State Key Laboratory of Green Chemical Engineering and Industrial Catalysis, Sinopec Shanghai Research Institute of Petrochemical Technology, Shanghai 201208, China

ARTICLE INFO

Article history:
Received 9 April 2020
Revised 27 October 2021
Accepted 2 November 2021
Available online 2 June 2022

Keywords:
Dry reforming of ethane
Strong metal–support interaction
Carbon dioxide
Ceria
Oxygen vacancy
Reaction mechanism

ABSTRACT

Dry reforming of ethane (DRE) has received significant attention because of its potential to produce chemical raw materials and reduce carbon emissions. Herein, a composition-induced strong metal–support interaction (SMSI) effect over FeNi/Al–Ce–O catalysts is revealed via X-ray photoelectron spectroscopy (XPS), H_2-temperature programmed reduction (TPR), and energy dispersive X-ray spectroscopy (EDS) elemental mapping. The introduction of Al into Al–Ce–O supports significantly influences the dispersion of surface active components and improves the catalytic performance for DRE over supported FeNi catalysts due to enhancement of the SMSI effect. The catalytic properties, for example, C_2H_6 and CO_2 conversion, CO selectivity and yield, and turnover frequencies (TOFs), of supported FeNi catalysts first increase and then decrease with increasing Al content, following the same trend as the theoretical effective surface area (TESA) of the corresponding catalysts. The FeNi/Ce–$Al_{0.5}$ catalyst, with 50% Al content, exhibits the best DRE performance under steady-state conditions at 873 K. As observed by with *in situ* Fourier transform infrared spectroscopy (FTIR) analysis, the introduction of Al not only increases the content of surface Ce^{3+} and oxygen vacancies but also promotes the dispersion of surface active components, which further alters the catalytic properties for DRE over supported FeNi catalysts.

1. Introduction

Excessive carbon dioxide (CO_2) emissions caused by human activities, for example, the consumption of fossil fuels, deforestation, and forest degradation, have been considered the major culprit of climate change and ocean acidification [1–3]. In the past decade, shale gas has set off a global energy revolution. Especially in the United States, shale gas has become the most important source of natural gas. With CO_2 as a soft oxidant, ethane (C_2H_6), the second most abundant component (approximately 10% of the content) of shale gas, can be converted into important raw materials [4]. Generally, the reaction between C_2H_6 and CO_2 occurs via two distinct pathways: ① dry reforming of ethane (DRE) into syngas through cleavage of the C–C bond ($C_2H_6 + 2CO_2 \rightarrow 4CO + 3H_2$); and ② oxidative dehydrogenation of ethane (ODHE) into ethylene (C_2H_4) by blocking cleavage of the C–C bond ($C_2H_6 + CO_2 \rightarrow C_2H_4 + CO + H_2O$) [5–7]. Syngas, a mixture of hydrogen (H_2) and carbon monoxide (CO), is an important feedstock for fuels and chemicals and is conventionally produced by steam reforming or partial oxidation of natural gas, liquefied gas, naphtha, and so on [8–10] or dry reforming of methane (DRM) [11–14]. However, the above processes are highly endothermic, with high energy consumption, and most DRM catalysts suffer deactivation due to coke formation and active site sintering at high operation temperatures above 1000 K [6,15–17]. A reaction temperature at least 100 K lower for DRE enables the production of syngas and the reduction of catalyst deactivation under milder conditions [5,6].

Ni-based catalysts, especially supported Ni catalysts, are widely used in DRM because of their high catalytic activity [12,18–22]. However, Ni-based catalysts suffer from deactivation due to poor coke resistance and particle sintering. Thus, alloying Ni with transition metals (Co, Ru, Pd, Pt) [21,23–25], developing advanced supports [26–28], and using alkali cations as promoters [29–31] have been investigated to overcome the drawbacks of traditional Ni-based catalysts. Because of the broad application prospects in producing chemicals and fuels at operation temperatures below 900 K, DRE has drawn much attention, and a series of catalysts have been developed, including trimetallic perovskites [32,33], supported Pt-based bimetallic catalysts [5,6,17], and supported

* Corresponding author.
E-mail address: yangwm.sshy@sinopec.com (W.-M. Yang).

https://doi.org/10.1016/j.eng.2021.11.027

Ni composite catalysts [34,35]. The strong metal–support interaction (SMSI) effect has been proven to have a significant impact on the catalytic performance of Ni-based catalysts for DRM and DRE. Ceria (CeO_2) supports with more oxygen vacancies show a stronger SMSI effect, which not only improves the dispersion of Ni species but also enhances the bonding between Ni species and the CeO_2 supports [36,37]. Liu et al. [38] reported the SMSI effect between small Ni nanoparticles (NPs) and partially reduced CeO_2. CO_2 adsorbs and dissociates at oxygen vacancies to generate CO and active oxygen. The synergy between Ni and active oxygen reduces the activation barrier of CH_4 bond dissociation and generates CH_x (x = 2, 3) species on the surface of the Ni/CeO_2 catalyst, making the dissociation temperature of CH_4 as low as 700 K. Lustemberg et al. [39] further proved the important role of Ce^{3+} in the dissociation of C–H bonds. Smaller Ni particles on the CeO_2 support experience larger electronic perturbations, resulting in a more significant binding energy and a lower activation barrier for the first C–H bond cleavage. Recently, Xie et al. [40] investigated the effects of oxide supports for DRE over both reducible and irreducible oxide-supported Pt–Ni bimetallic catalysts. The DRE performance over the PtNi/CeO_2 catalyst was greatly improved because the reducible CeO_2 effectively activated CO_2 and promoted the dissociation of C_2H_6 through a bifunctional Mars–van Krevelen redox mechanism.

Moreover, the dry reforming process is always accomplished by the reverse water–gas shift (RWGS) reaction with a low activation barrier [13,17,40,41]. It has been proven that the introduction of Al into CeO_2 promotes the formation of oxygen vacancies, which inhibits the RWGS reaction because of the powerful activation and dissociation capacity of CO_2 [13,42]. FeO_x has also been reported to be a promoter of supported Ni catalysts for both the RWGS reaction [43] and DRM [44] due to the enhancement of Ni dispersion and the formation of Ni-rich NiFe alloys. Recently, Yan et al. [45] reported the adjustment of active interfacial sites by changing the composition of FeNi active components, which was shown to greatly influence the selectivity toward ODHE or DRE. Herein, we consider an FeNi/CeO_2 catalyst with high ethylene selectivity as the initial system and adjust the distribution of surface active components by introducing Al into the CeO_2 support to obtain high-performance catalysts for DRE.

In this article, we synthesized a series of FeNi/Al–Ce–O catalysts with an enhanced SMSI effect via a facile sol–gel and impregnation method and investigated the catalytic properties for DRE over supported FeNi catalysts under steady-state reaction conditions. The enhanced SMSI effect between the surface active components and Al–Ce–O supports and its influences were confirmed via X-ray photoelectron spectroscopy (XPS), H_2-temperature programmed reduction (TPR), and energy dispersive X-ray spectroscopy (EDS) element mapping. This work also proposes a possible reaction mechanism and the corresponding adsorbed intermediates over supported FeNi catalysts via *in situ* Fourier transform infrared (FTIR) spectra under the reaction conditions. We established a relationship between catalytic properties and surface structure over supported FeNi catalysts, which will greatly contribute to the research on related catalytic systems.

2. Experimental methods

2.1. Catalyst preparation

2.1.1. Materials

Pluronic® F127 ($EO_{106}PO_{70}EO_{106}$, M_w = 12 600) was purchased from Sigma-Aldrich Chemical Inc. (USA). $Ce(NO_3)_3{\cdot}6H_2O$ (analytical reagent (AR), 99.0%), $Al(NO_3)_3{\cdot}9H_2O$ (AR, 99.0%), $Ni(NO_3)_2{\cdot}6H_2O$ (AR, 98.0%), quartz sand (25–50 mesh, AR, 95.0%), and absolute ethanol (AR, 99.7%) were purchased from Sinopharm Chemical Reagent Co., Ltd. (China). $Fe(NO_3)_3{\cdot}9H_2O$ (AR, 98.5%) was purchased from Nanjing Chemical Reagent Co., Ltd. (China). All the chemicals were used as received.

2.1.2. Synthesis of Al–Ce–O supports

Al–Ce–O supports were synthesized via a facile sol–gel process combined with evaporation-induced self-assembly (EISA) in ethanol using F127 as the template, which provides a large specific surface area and superior catalytic performance [13,46–49]. In a typical synthesis, 1.6 g of F127 was dissolved in 40 mL of ethanol at room temperature (RT). A total of 10.0 mmol of metal precursors ($Ce(NO_3)_3{\cdot}6H_2O$ and $Al(NO_3)_3{\cdot}9H_2O$) with an Al molar ratio between 10% and 90% (10% increment of each sample) were added into the above solution with vigorous stirring. The mixture was covered with polyethylene (PE) film and stirred for at least 5 h at RT. The homogeneous sol was then transferred into an oven and underwent solvent evaporation. After aging at 313 and 333 K for 24 h successively, the gel product was dried in an oven at 373 K for another 24 h. Calcination was performed by slowly increasing the temperature from RT to 923 K (2 K·min^{-1} ramping rate) and then heating at 923 K for 4 h in air. The CeO_2 and Al_2O_3 supports were synthesized via the same procedure except the mixed metal precursors were replaced with 10.0 mmol of $Ce(NO_3)_3{\cdot}6H_2O$ (4.34 g) or $Al(NO_3)_3{\cdot}9H_2O$ (3.75 g), respectively. The yellow or white products were then ground into a powder.

2.1.3. Synthesis of supported FeNi bimetallic catalysts

Supported FeNi bimetallic catalysts were synthesized via an incipient wetness impregnation method over as-synthesized CeO_2, Al_2O_3, and Al–Ce–O supports [6,40,45]. In a typical synthesis, a bimetallic co-impregnation procedure was used to maximize the interaction between the two metals. Precursor solutions were prepared by dissolving 101 mg of $Fe(NO_3)_3{\cdot}9H_2O$ and 83 mg of $Ni(NO_3)_2{\cdot}6H_2O$ in a specific amount of deionized water sufficient to fill the pores of 0.981 g of corresponding metal oxide support, the pore volume of which was determined by means of nitrogen adsorption measurements. The solution was added dropwise to the support with thorough stirring. The loadings of bimetallic active components were 1.15 wt% for Fe and 0.40 wt% for Ni to obtain a 3:1 molar ratio of Fe/Ni. The catalyst was then dried at 353 K for 12 h and calcined at 723 K for 4 h with a ramping rate of 2 K·min^{-1} from RT to 723 K. Since the FeNi/CeO_2 catalyst with an Fe/Ni molar ratio of 3:1 shows high ethylene selectivity due to its special Ni–FeO_x interfacial sites [45], such active metal components would better reflect the enhanced SMSI effect of Al–Ce–O supports on the catalytic properties.

2.2. Catalyst characterization

Powder X-ray diffraction (XRD) analysis was performed on a Bruker D8 Advance SS diffractometer (Bruker Corporation, USA) operated at 40 kV and 40 mA with a slit of 0.5° at a 2θ scanning speed of 2°·min^{-1} under a Cu-Kα source (0.15432 nm). Nitrogen adsorption–desorption isotherms were measured at 77 K using a Micromeritics ASAP 2010 analyzer (Micromeritics Instrument Corporation, USA). The Brunauer–Emmett–Teller (BET) specific surface area was measured after degassing the samples at 373 and 623 K for 3 h successively under vacuum. The elemental composition of the supported FeNi catalysts was determined by inductively coupled plasma-atomic emission spectrometry (ICP-AES; Varian Vista AX, Varian Inc., USA). ^{27}Al magic-angle spinning nuclear magnetic resonance (MAS NMR) spectroscopy was conducted with a Varian VNMRS-400WB nuclear magnetic resonance instrument (Varian Inc., USA) with a frequency of 104.18 MHz, a spinning speed of 10 000 Hz, and a relaxation delay of 4 s. Chemical shift values are

reported with respect to $KAl(SO_4)_2{\cdot}12H_2O$ as the standard. XPS was performed on a Thermo ESCALAB 250 spectrometer (Thermo Fisher Scientific Inc., USA) with a monochromatic Al-Kα X-ray source (1486.6 eV, 1 eV = 1.602176×10^{-19} J) and an analyzer pass energy of 20 eV. The C 1s line at 284.6 eV was used to calibrate the binding energies (BEs) of the measured elements.

H_2-TPR experiments were conducted on a Micromeritics AutoChem II 2920 chemisorption analyzer (Micromeritics Instrument Corporation, USA). In a typical experiment, 50 mg of the as-synthesized catalyst was put into a U-shaped quartz tube and pretreated in a 50 mL·min^{-1} He flow at RT. Then, the TPR experiment was performed under a 10 vol% H_2/Ar mixture at a space velocity of 50 mL·min^{-1} with a ramping rate of 10 K·min^{-1} from RT to 1173 K. Pulse CO chemisorption experiments were also performed on a Micromeritics AutoChem II 2920 chemisorption analyzer to measure the CO uptake value of the catalyst. Approximately 150 mg of the catalyst was first reduced at 873 K in a 10 vol% H_2/Ar flow for 30 min. Then, the reduced catalyst was purged in a He flow until the temperature was decreased to 313 K. The loop gas of 10% CO/He (590 μL) was pulsed with a He stream over the catalyst until the peak area of CO became constant. The CO uptake values of the catalysts could provide an approach to estimate the turnover frequency (TOF), as reported previously [17,33,45].

Transmission electron microscopy (TEM), high-resolution transmission electron microscopy (HRTEM), high-angle annular dark field scanning transmission electron microscopy (HAADF-STEM), and EDS element mapping were conducted on an FEI Talos F200X TEM (Thermo Fisher Scientific Inc., USA) with a probe aberration corrector operating at 300 kV. The TEM samples were prepared by drying a drop of the sample dispersion in ethanol on carbon-coated copper grids.

In situ FTIR spectra were obtained on a Bruker Vertex 70 V FTIR spectrometer (Bruker Corporation, USA) with a stainless steel high-vacuum transmission infrared cell. The samples were pressed on a tungsten mesh support and heated to 623–673 K at a ramping rate of 10 K·min^{-1} under vacuum for 2 h to remove the surface adsorbed water. The background spectra were collected after the tungsten mesh support was cooled to RT. In a typical *in situ* infrared (IR) experiment under the reaction conditions, 1.0 mbar (1 mbar = 100 Pa) of C_2H_6 and 1.0 mbar of CO_2 were introduced into the cell, and IR spectra of each sample were collected in the temperature range of 373–873 K. *In situ* CO adsorption IR spectra of the FeNi/Ce–$Al_{0.5}$ catalyst were collected under a CO pressure of 5.0 mbar from 373 to 573 K and 1.0 mbar from 673 to 873 K.

2.3. Catalytic performance evaluations

The catalytic performance of supported FeNi bimetallic catalysts was evaluated in a continuous-flow fixed-bed quartz tabular reactor (7.5 mm inner diameter) under atmospheric pressure, utilizing a mixture of 100 mg of catalyst (20–40 mesh) and 100 mg of quartz sand loading between two quartz wool plugs at the center of the reactor. The catalyst was pretreated *in situ* with 40 mL·min^{-1} H_2 at 673 K for 1 h and then heated to 873 K at a ramping rate of 5 K·min^{-1} with a constant total flow rate of C_2H_6, CO_2, and N_2 of 40 mL·min^{-1}. The volume ratio of the C_2H_6, CO_2, and N_2 mixed gas was 1:1:2. The temperature of the catalyst bed was held at 873 K for 8 h, and the outlet stream was analyzed online using a gas chromatograph (Agilent 6820B, Agilent Technologies, Inc., USA) with a thermal conductivity detector (TCD). Water within the outlet stream was removed by a condenser. N_2 was used as an internal standard to account for the volume effects due to the high temperature during the reaction. Blank experiments without supported FeNi catalysts were conducted at 873 K to evaluate the contribution of the gas-phase reaction and system, and the results showed a negligible effect on DRE performance. In this article, the steady-state conversion (X), TOF, C_2H_6-based selectivity (S), and yield (Y) of species i were defined using the following equations:

$$X_i = \frac{F_{i,\text{in}} - F_{i,\text{out}}}{F_{i,\text{in}}} \times 100\% \quad (1)$$

$$\text{TOF}_i = \frac{F_{i,\text{in}} \cdot X_i}{U_{\text{CO}} \cdot m_{\text{cat}}} \quad (2)$$

$$S_i = \frac{F_{i,\text{out}}}{F_{C_2H_6,\text{in}} - F_{C_2H_6,\text{out}}} \cdot \frac{N_{i,C}}{N_{C_2H_6,C}} \times 100\% \ (\text{i} \neq \text{CO}) \quad (3)$$

$$S_{\text{CO}} = 1 - \sum\nolimits_{i \neq \text{CO}} S_i \times 100\% \quad (4)$$

$$Y_i = X_{C_2H_6} \cdot S_i \quad (5)$$

where F_{in} and F_{out} are the inlet and outlet flow rates of the reactant (mol·min^{-1}), U_{CO} is the CO uptake value (mol·g^{-1}), m_{cat} is the mass of the catalyst (g), and N_C is the carbon atom number of the products.

3. Results and discussion

3.1. Structural characterizations

Powder XRD patterns of the as-synthesized catalysts with standard Joint Committee on Powder Diffraction Standards (JCPDS) cards are shown in Fig. 1. The diffraction peaks of FeNi/Ce–Al_x ($x \leq 70\%$) and FeNi/CeO_2 confirm the fluorite cubic structure of CeO_2 ($Fm\bar{3}m$, JCPDS 75-0120), while the pattern of FeNi/Al_2O_3 is consistent with the structure of η-Al_2O_3 ($Fd\bar{3}mS$, JCPDS 77-0396). FeNi/Ce–$Al_{0.9}$ shows significant phase separation into CeO_2, η-Al_2O_3, and $Al(OH)_3$ ($P1(1)$, JCPDS 24–0006). No peaks attributed to Fe and Ni are observed in these patterns. As shown in Table 1, the average crystallite size of the catalysts calculated by the Scherrer equation [50] significantly decreases with increasing Al content, which indicates that Al improves the sintering resistance of the CeO_2 supports [47]. The size distributions of supported FeNi catalysts were further estimated by the size statistics of NPs from TEM images. The TEM and HRTEM images of supported FeNi catalysts are shown in Figs. S1

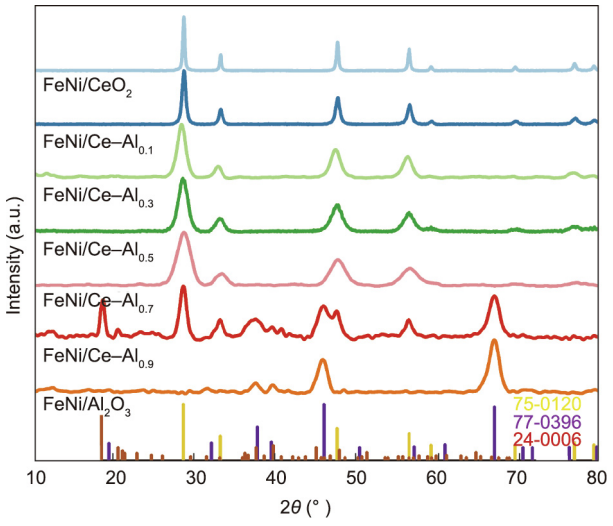

Fig. 1. XRD patterns of as-synthesized supported FeNi catalysts. The standard XRD patterns of CeO_2 ($Fm\bar{3}m$, JCPDS 75-0120), η-Al_2O_3 ($Fd\bar{3}mS$, JCPDS 77-0396), and $Al(OH)_3$ ($P1(1)$, JCPDS 24-0006) are shown in the panel as a reference. a.u.: arbitrary unit.

Table 1
Average crystallite size (XRD size), crystal microstrain, lattice parameter, TEM size distribution data, and BET surface area (S_{BET}) of supported FeNi catalysts.

Catalysts	XRD size (nm)[a]	Microstrain (%)[a,b]	Lattice parameter (Å)[a]	TEM size (nm)	S_{BET} ($m^2 \cdot g^{-1}$)
$FeNi/CeO_2$	27.3	0.50	5.40(1)	31.8 ± 6.7	15.3
$FeNi/Ce–Al_{0.1}$	15.7	0.89	5.39(7)	17.0 ± 3.4	17.9
$FeNi/Ce–Al_{0.3}$	10.1	1.43	5.44(9)	11.6 ± 1.8	55.2
$FeNi/Ce–Al_{0.5}$	8.7	1.60	5.41(9)	8.6 ± 0.9	79.0
$FeNi/Ce–Al_{0.7}$	8.1	1.62	5.40(1)	—	96.5
$FeNi/Ce–Al_{0.9}$	5.8	1.07	7.90(6)	—	111.8
$FeNi/Al_2O_3$	6.7	0.93	7.90(7)	—	125.5

[a] Calculated (440) diffraction peaks for $FeNi/Al_2O_3$ and $FeNi/Ce–Al_{0.9}$ and (111) diffraction peaks for other supported FeNi catalysts.
[b] Estimated via the single line method for analysis of XRD line broadening using a pseudo-Voigt profile function.

and S2 in Appendix A. The size distributions of the $FeNi/CeO_2$ and $FeNi/Ce–Al_x$ ($10\% \leq x \leq 50\%$) catalysts in Table 1 are close to the corresponding average crystallite sizes. As shown in Table 1 and Fig. S3 in Appendix A, the BET specific surface area of supported FeNi catalysts is positively related to the Al content. The average crystallite size of the $FeNi/Ce–Al_x$ ($70\% \leq x \leq 90\%$) catalysts becomes even smaller upon formation of a mesoporous structure, as shown in Fig. S2, which reveals the relationship between the size distribution and BET specific surface area of supported FeNi catalysts. In Figs. S1 and S2, lattice spacings of 3.12, 2.71, 1.91, and 2.38 Å correspond to the (111), (200), and (220) facets of CeO_2 and (311) facet of η-Al_2O_3, respectively. The lattice spacing of $FeNi/Ce–Al_{0.9}$ is indistinguishable owing to the poor crystallinity and severe phase separation.

To further discuss the microstructure of the catalysts, the microstrains and lattice parameters were calculated, and the results are listed in Table 1. The microstrain in the lattice (lattice strain) of the samples was estimated via the single line method for analysis of XRD line broadening using a pseudo-Voigt profile function [51,52]. As shown in Fig. 1, for the $FeNi/CeO_2$ and $FeNi/Ce–Al_x$ ($10\% \leq x \leq 70\%$) catalysts with fluorite cubic structures, the microstrain in the crystal lattice of the oxide supports increases as a function of Al content to maintain the original crystal structure. The lattice distortion is relieved by a decrease in the microstrain and phase transition after the introduction of a high content of Al. The lattice parameters determined via Bragg's law from the (111) diffraction peak of CeO_2 ($Fm\bar{3}m$, JCPDS 75-0120) for $FeNi/CeO_2$ and $FeNi/Ce–Al_x$ ($10\% \leq x \leq 70\%$) as well as the (440) peak of η-Al_2O_3 ($Fd\bar{3}mS$, JCPDS 77-0396) for $FeNi/Ce–Al_{0.9}$ and $FeNi/Al_2O_3$ are also listed in Table 1. Fig. S4 in Appendix A shows the ^{27}Al MAS NMR spectra of $FeNi/Ce–Al_x$ ($10\% \leq x \leq 50\%$) and of $FeNi/Al_2O_3$. The peaks at approximately 8 and 66 ppm are assigned to octahedrally (Al_{oct}) and tetrahedrally (Al_{tet}) coordinated Al^{3+}, while the Al species with a chemical shift of 38 ppm is a CeO_2 lattice occupied by Al^{3+} [53]. The increased peak intensity at 38 ppm for $FeNi/Ce–Al_{0.1}$ and $FeNi/Ce–Al_{0.3}$ is a result of Al^{3+} ions present in the CeO_2 lattice. The similarity of the spectra of $FeNi/Ce–Al_{0.5}$ and $FeNi/Al_2O_3$ indicates a stable octahedral coordination of Al^{3+} species with a high content of Al in $FeNi/Ce–Al_x$ ($50\% \leq x \leq 90\%$). Regardless of the phase transition, the change in the lattice parameter of the supports is mainly related to two factors: ① the formation of oxygen vacancies by replacing Ce^{4+} with Al^{3+}, which leads to crystal lattice shrinkage, and ② the transition from Ce^{4+} to Ce^{3+} with a corresponding reduction in the ionic radius, which is essential to balance the electric charge of the unit cell. The change in the lattice parameter is thought to be a result of the synergistic effect of the two factors: the formation of surface oxygen vacancies and Ce^{3+} species.

3.2. Catalytic performance

The steady-state catalytic performance of the FeNi/Al–Ce–O catalysts at 873 K is shown in Figs. 2 and 3, where the $FeNi/CeO_2$ and $FeNi/Al_2O_3$ catalyst data were also plotted as a reference. The experimental data indicate that the composition of oxide supports plays an important role in the catalytic properties for DRE over supported FeNi catalysts. As shown in Figs. 2(a) and (b), C_2H_6 and CO_2 conversion is positively correlated with the Al content ($0 \leq x \leq 50\%$), whereas completely opposite trends are observed in Figs. 3(a) and (b) when the Al content is above 50%. In Fig. S5 in Appendix A, the CO selectivity from C_2H_6 also significantly increases with increasing Al content ($0 \leq x \leq 30\%$), while the ethylene selectivity decreases correspondingly. As the Al content changes between 30% and 90%, the CO selectivity of the FeNi/Al–Ce–O catalysts remains stable at 96%–98%. In Figs. 2(c) and 3(c), the CO yield from C_2H_6 over the FeNi/Al–Ce–O catalysts follows the same trend of first increasing and then decreasing with increasing Al content. The $FeNi/Ce–Al_{0.5}$ catalyst provides the best DRE performance, with the highest C_2H_6 and CO_2 conversions and CO selectivity and yield. The introduction of Al into CeO_2 possibly enhances the interaction between the surface active components and the Al–Ce–O support, which further affects the catalytic properties over supported FeNi catalysts.

The average catalytic performance data of the supported FeNi catalysts between 420 and 480 min are summarized in Table 2. After several hours of steady-state reaction, the C_2H_6 and CO_2 conversion, CO selectivity, and CO yield over the supported FeNi catalysts maintain the same relative order. The $FeNi/Ce–Al_{0.5}$ catalyst exhibits the best DRE performance with the highest C_2H_6 conversion (11.7%), CO_2 conversion (33.1%), and CO yield (11.5%). The TOF values based on CO uptake also indicate the outstanding catalytic activity of the $FeNi/Ce–Al_{0.5}$ catalyst for both C_2H_6 ($47.1\ min^{-1}$) and CO_2 ($133.1\ min^{-1}$). As a comparison, the catalytic performance data of recently reported DRE catalysts are listed in Table S1 in Appendix A. The $FeNi/Ce–Al_{0.5}$ catalyst shows high TOFs and CO selectivity similar to other high-performance DRE catalysts, whereas the conversions are possibly restricted by the low loading of bimetallic active components. Catalysts with Al contents above 50% show lower TOF values for both C_2H_6 and CO_2 in this reaction, which demonstrates that the enhancement of DRE performance over the $FeNi/Ce–Al_{0.5}$ catalyst should be attributed not only to the increasing Al content but also to the interaction between surface active components and the Al–Ce–O support. H_2/CO molar ratios lower than 0.75 due to the side reaction of the RWGS are also shown in Table 2 [33]. The highest H_2/CO ratio of the $FeNi/Ce–Al_{0.5}$ catalyst indicates that the SMSI effect enhanced by the introduction of Al partially inhibits the RWGS process in this reaction, which is also related to the surface oxygen vacancy over the FeNi/Al–Ce–O catalysts.

3.3. Surface composition analysis

The elementary composition and chemical valence on the surface of hydrogen-reduced catalysts were detected via XPS. Typical Ce 3d and Al 2p core level spectra of the $FeNi/CeO_2$, FeNi/Al–Ce–O, and $FeNi/Al_2O_3$ catalysts are shown in Appendix A Fig. S6. During typical data processing, the complex spectra of the samples in

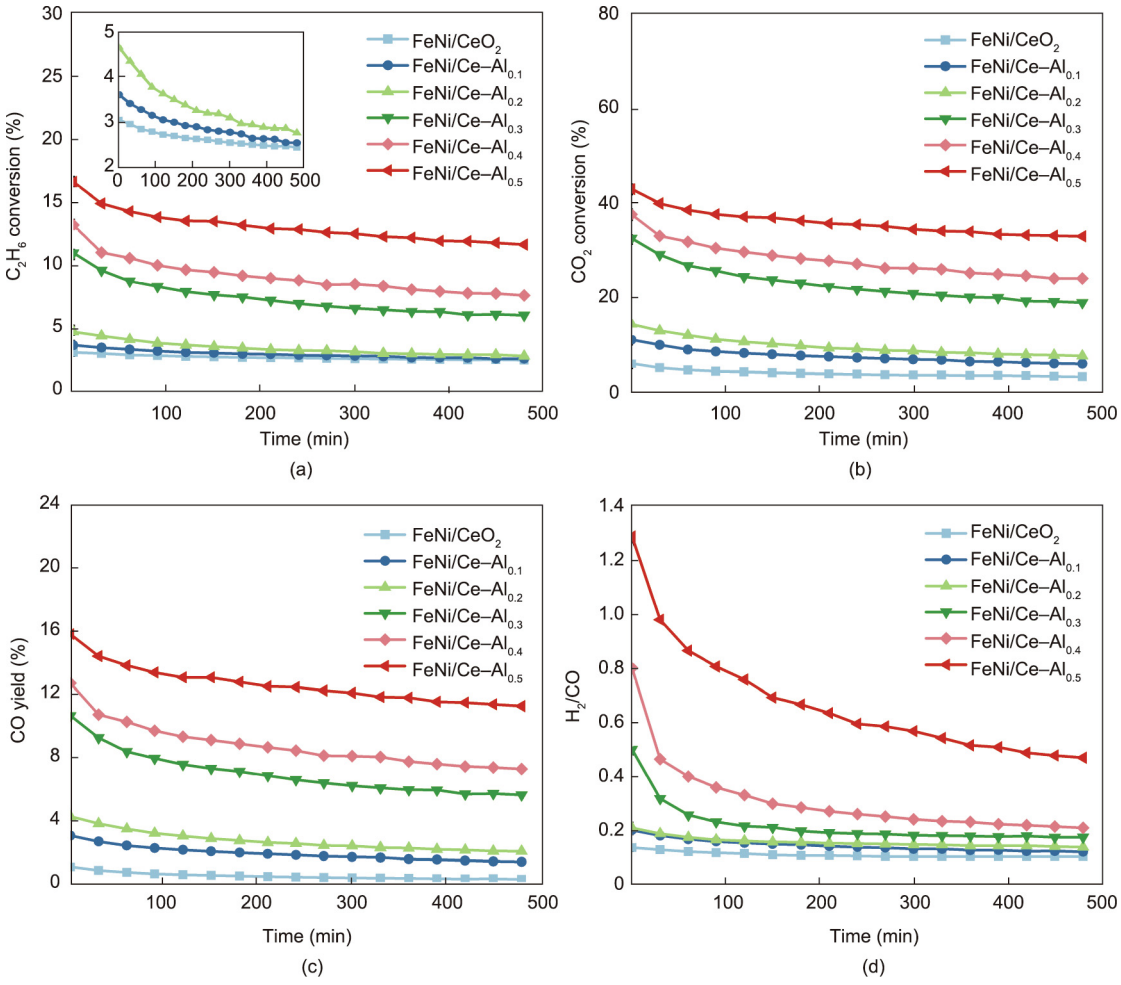

Fig. 2. (a) C_2H_6 conversion, (b) CO_2 conversion, (c) CO yield, and (d) H_2/CO molar ratio over FeNi/Ce–Al_x ($10\% \leq x \leq 50\%$) and FeNi/CeO_2 catalysts under steady-state reaction conditions at 873 K and 1 atm (1 atm = 1.01325 × 10^5 Pa) with a flow rate of 40 mL·min^{-1} (C_2H_6:CO_2:N_2 = 1:1:2) and gas hourly space velocity (GHSV) of 24 000 mL·(h·g)$^{-1}$.

the Ce 3d region were deconvoluted into ten components via the generally accepted approach of extracting the ratio of Ce^{3+} and Ce^{4+} [54,55]. The ten peaks contained five spin-orbital split pairs of Ce $3d_{5/2}$ (v^i: v_0, v, v', v'', and v''') and Ce $3d_{3/2}$ (u^i: u_0, u, u', u'', and u'''), of which the area intensities, the full widths at half-maximum (FWHM), and the position distances were fixed as constants during the deconvolution. Herein, the peak positions are marked in Fig. S6(a); the relative contents of Ce^{3+} to the total Ce content (c_{Ce})in the samples were calculated via the following equation, and the results are listed in Table 3:

$$\frac{c_{Ce^{3+}}}{c_{Ce}} = \frac{I_{v_0} + I_{v'} + I_{u_0} + I_{u'}}{\sum_i (I_{v^i} + I_{u^i})} \times 100\% \quad (6)$$

where $c_{Ce^{3+}}$ is the content of Ce^{3+}, and I is the area intensity of the given component. As shown in Table 3, the surface relative content of Ce^{3+} increases significantly with Al content. Shyu et al. [56] reported that the area under the u''' peak in the total Ce 3d region could be used to describe the relative content of Ce^{4+} in the samples. In Table 3, it is observed that the area under the u''' peak shows a negative relationship with the Al content, which also confirms the correlation above. Herein, the theoretical effective surface area (TESA, S_{eff}) of supported FeNi catalysts is defined by the following equation:

$$S_{eff} = S_{BET} \cdot P_{r,\,Ce^{3+}} \cdot P_{Ce} \quad (7)$$

where S_{BET} is the BET specific surface area of the catalyst, $P_{r,Ce^{3+}}$ is the relative surface content of Ce^{3+}, and P_{Ce} is the total surface content of Ce of the catalyst. According to the data in Table 3, as the Al content increases, the TESA shows the same trend as the conversions and TOFs of C_2H_6 and CO_2, indicating that the reactivity of C_2H_6 with CO_2 is closely related to the content of surface Ce^{3+} species over supported FeNi catalysts. Moreover, the dispersion of surface active components should be another important factor to be discussed later. In Fig. S6, the binding energy of the Ce 3d core level of the FeNi/Al–Ce–O catalysts decreases slightly with increasing Al content compared with that of FeNi/CeO_2. In addition, the peaks of the Al 2p core level of the FeNi/Al–Ce–O catalysts shift to lower binding energies than that of FeNi/Al_2O_3 with increasing Ce content, which demonstrates electron transfer between Ce or Al and adjacent atoms.

Fig. S7 in Appendix A shows the O 1s and Fe 2p XPS spectra of the reduced FeNi catalysts. In Fig. S7(a), the binding energies at approximately 529.2 and 531.7 eV are ascribed to the lattice oxygen of Ce-based oxides (O_I) and the adsorbed oxygen or hydroxyl groups (O_{II}) on the surface, respectively [41,57,58]. The O 1s core level binding energy of Al_2O_3 is located at 530.9 eV [57]. The O_{II}/O_I ratios in Table 3 increase gradually with increasing Al content, which indicates an increase in surface oxygen vacancies over the FeNi/Al–Ce–O catalysts [13,41]. In Fig. S7(b), the Fe 2p core level binding energies of the reduced FeNi catalysts at approximately 710.9 and 724.0 eV are ascribed to Fe_2O_3, which means that the surface Fe species should be highly oxidized during the reaction [57]. Raman spectroscopy was also conducted to determine the surface oxygen vacancy of the catalysts. Fig. S8 in Appendix A

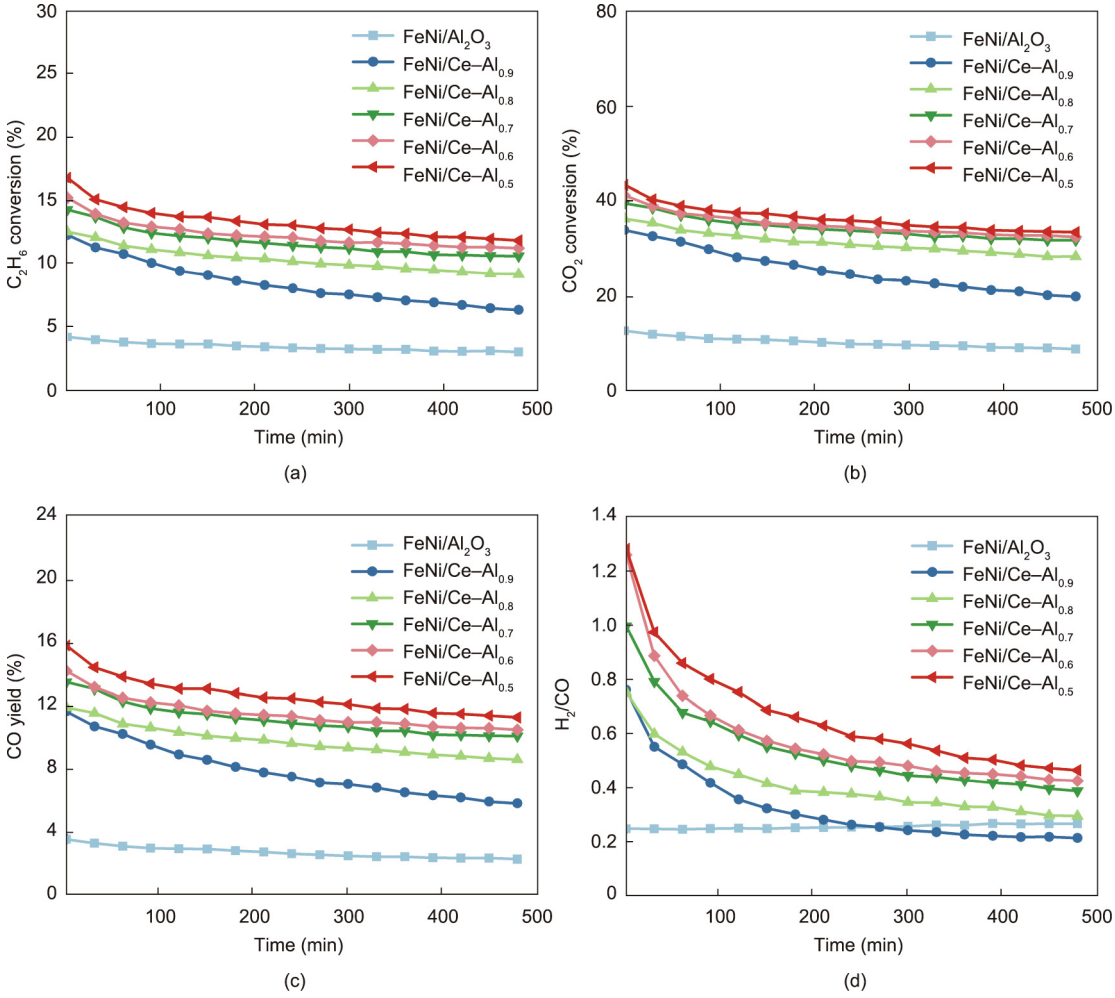

Fig. 3. (a) C_2H_6 conversion, (b) CO_2 conversion, (c) CO yield, and (d) H_2/CO molar ratio over FeNi/Ce–Al_x ($50\% \leq x \leq 90\%$) and FeNi/Al_2O_3 catalysts under steady-state reaction conditions at 873 K and 1 atm with a flow rate of 40 mL·min^{-1} (C_2H_6:CO_2:N_2 = 1:1:2) and GHSV of 24 000 mL·(h·g)$^{-1}$.

Table 2
Summary of CO uptake and catalytic performance over supported FeNi catalysts under steady-state reaction conditions averaged between 420 and 480 min at 873 K.

Catalysts	CO uptake (μmol·g^{-1})	Conversion (%)		CO selectivity (%)	CO yield (%)	TOF (min^{-1})		H_2/CO
		C_2H_6	CO_2			C_2H_6	CO_2	
FeNi/CeO_2	58.1	2.4	3.4	15.3	0.4	1.7	2.4	0.10
FeNi/Ce–$Al_{0.1}$	55.2	2.5	6.1	59.1	1.5	1.9	4.6	0.12
FeNi/Ce–$Al_{0.3}$	38.5	6.0	19.1	95.9	5.8	6.5	20.6	0.17
FeNi/Ce–$Al_{0.5}$	10.4	11.7	33.1	97.7	11.5	47.1	133.1	0.48
FeNi/Ce–$Al_{0.7}$	10.2	10.4	31.4	98.1	10.2	42.4	128.1	0.40
FeNi/Ce–$Al_{0.9}$	20.7	6.2	19.8	96.8	6.0	12.6	39.9	0.22
FeNi/Al_2O_3	32.9	2.8	8.4	86.1	2.4	3.5	10.6	0.27

Table 3
Relative surface content of Ce^{3+}, area under the u''' peak, total surface content of Ce, TESA (S_{eff}), and O_{II}/O_I ratio of O 1s core level over supported FeNi catalysts.

Catalysts	Ce^{3+}/Ce (%)	u'''/Ce (%)	Ce/(Ce + Al) (%)	S_{eff} (m^2·g^{-1})	O_{II}/O_I
FeNi/CeO_2	19.5	12.9	100.0	3.0	0.32
FeNi/Ce–$Al_{0.1}$	22.4	10.9	78.9	3.2	0.35
FeNi/Ce–$Al_{0.3}$	23.9	10.8	69.5	9.2	0.41
FeNi/Ce–$Al_{0.5}$	34.4	9.4	56.6	15.4	0.49
FeNi/Ce–$Al_{0.7}$	38.1	8.8	35.6	13.1	0.73
FeNi/Ce–$Al_{0.9}$	52.5	4.4	12.1	7.2	0.97

shows the Raman spectra of the supported FeNi catalysts excited by a 532 nm laser. The strong band at approximately 462 cm^{-1} is ascribed to the F_{2g} vibration mode of the Ce–8O vibrational unit of the fluorite structure, while the weak bands at approximately 254 and 596 cm^{-1} are attributed to the second-order transverse acoustic (2TA) mode and the defect-induced (D) mode of oxygen vacancies, respectively. The relative intensity ratio I_D/I_{F2g} reflects the content of oxygen vacancies [59,60]. As seen in Fig. S8, the intensity ratio of I_D/I_{F2g} increases slightly with Al content, which also indicates that the introduction of Al improves the content of surface oxygen vacancies and the inhibition of the RWGS reaction over the FeNi/Al–Ce–O catalysts. According to the results above, the introduction of Al into the CeO_2 support leads to a higher density of surface Ce^{3+} species and oxygen vacancies, which further improves the catalytic performance for DRE over FeNi/Al–Ce–O catalysts.

3.4. Active site investigation

The H_2-TPR profiles of the as-synthesized FeNi catalysts are shown in Fig. 4. To assign the peaks in the pattern, profiles of the as-synthesized Ce–$Al_{0.5}$ supported monometallic catalysts and pure CeO_2 support are also shown in Fig. S9 in Appendix A as a comparison. As seen in Fig. S9, CeO_2 reduction can be divided into two stages. The first short and wide peak located between 600 and 800 K is assigned to the reduction of surface active oxygen of CeO_2, which leads to the formation of surface oxygen vacancies and non-stoichiometric CeO_x, and the second peak above 800 K is attributed to bulk CeO_2 reduction [61–63]. In Fig. 4, after adding surface active components to the support, a strong peak at approximately 550 K appears for the FeNi/CeO_2 catalyst. This peak can be attributed to the reduction of both surface active components and the CeO_2 support by surface hydrogen spillover [64]. Compared with the patterns of monometallic catalysts in Fig. S9, for the Ni/Ce–$Al_{0.5}$ catalyst, the peak below 673 K shows a lower reduction cutoff temperature than that of Fe/Ce–$Al_{0.5}$, which indicates that surface Ni species are much easier to reduce than Fe on Ce-based composite oxides. For the FeNi/Al–Ce–O catalysts, compared with the pattern for FeNi/CeO_2 in Fig. 4, the peak broadening and cutoff temperature rise also indicate that the introduction of Al significantly enhances the SMSI effect between surface active components and oxide supports.

To identify the dispersion of surface active components on the composite support, EDS elemental mapping measurements were conducted on three representative samples: FeNi/Ce–$Al_{0.1}$, FeNi/Ce–$Al_{0.5}$, and FeNi/Ce–$Al_{0.9}$. The element mapping images in this article are representatively chosen from many different regions of the samples. As shown in the EDS mapping images of Ce and Al in Figs. 5–7, Ce and Al are well distributed over the FeNi/Al–Ce–O catalysts. Nevertheless, the elemental distributions of Fe and Ni are quite different. Small bimetallic FeNi NPs are observed on the surface of FeNi/Ce–$Al_{0.1}$, as confirmed by the EDS mapping images shown in Fig. 5. Bimetallic FeNi NPs with similar structures have been proven to have high selectivity for ethylene [45]. As demonstrated by the gradual FeNi distribution changes shown in Figs. 6 and 7, as the Al content increases, the surface Fe and Ni species become well dispersed on the Al–Ce–O supports. The introduction of Al greatly increases the interaction between the surface active components and the composite support. The surface Fe

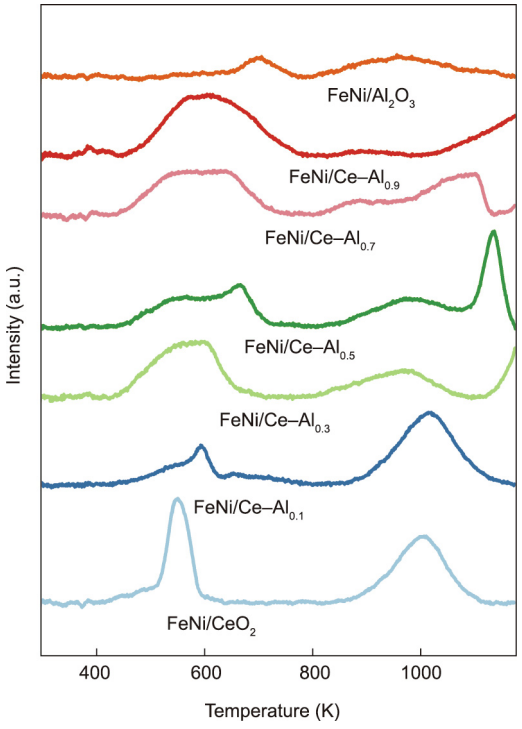

Fig. 4. H_2-TPR profiles of as-synthesized FeNi catalysts between 298 and 1173 K.

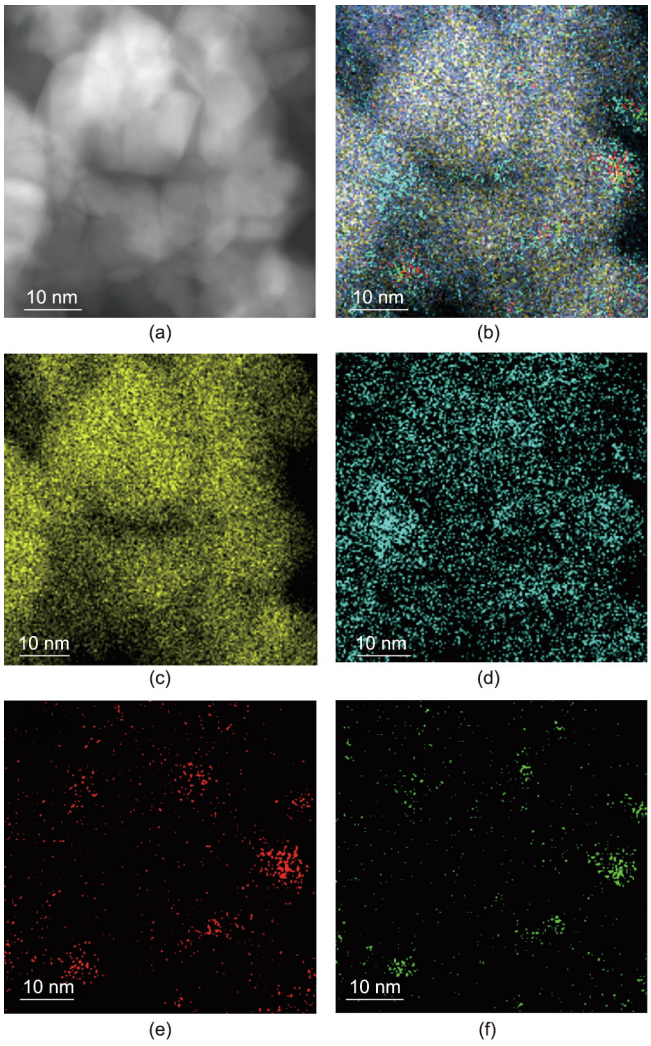

Fig. 5. (a) HAADF-STEM image. EDS mapping images: (b) overlay, (c) Ce, (d) Al, (e) Fe, and (f) Ni of the reduced FeNi/Ce–$Al_{0.1}$ catalyst with a scale bar of 10 nm.

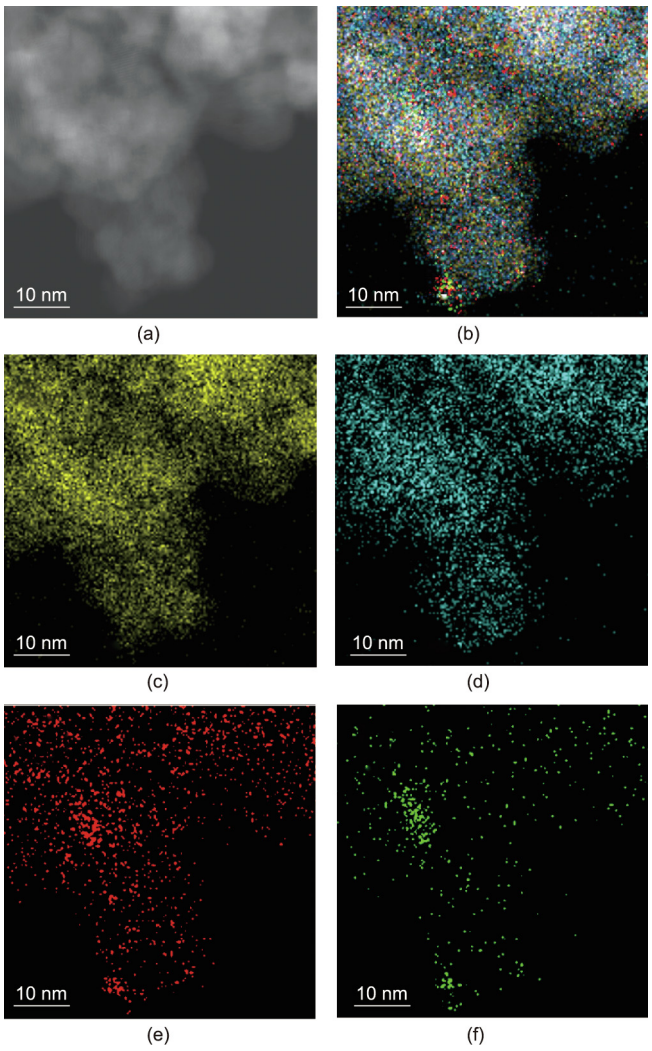

Fig. 6. (a) HAADF-STEM image. EDS mapping images: (b) overlay, (c) Ce, (d) Al, (e) Fe, and (f) Ni of the reduced FeNi/Ce–$Al_{0.5}$ catalyst with a scale bar of 10 nm.

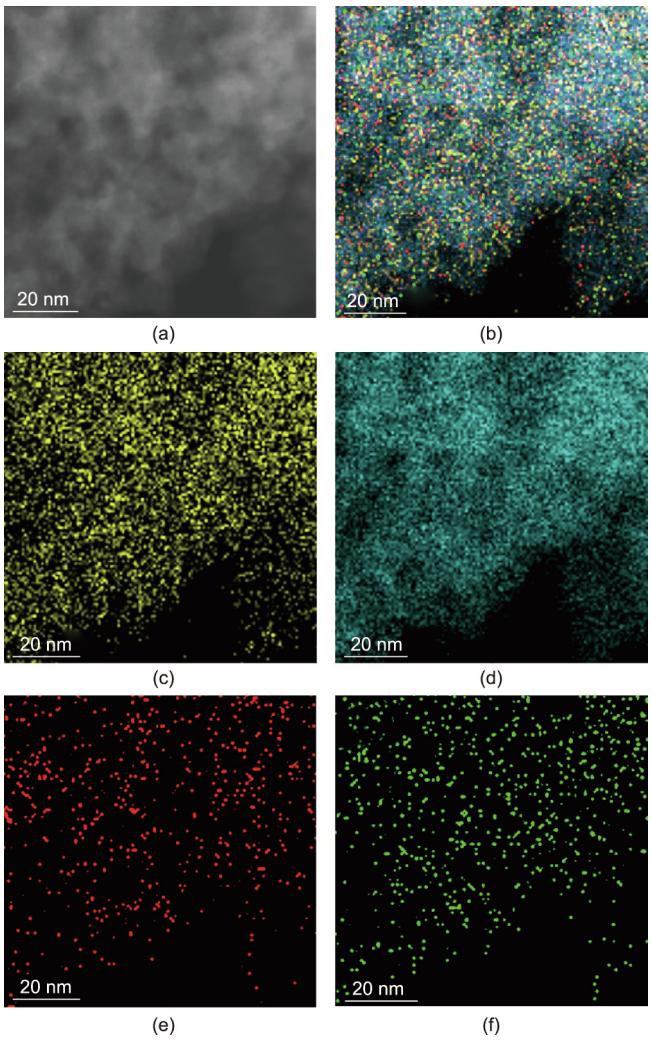

Fig. 7. (a) HAADF-STEM image. EDS mapping images: (b) overlay, (c) Ce, (d) Al, (e) Fe, and (f) Ni of the reduced FeNi/Ce–$Al_{0.9}$ catalyst with a scale bar of 20 nm.

and Ni species are dispersed randomly and independently throughout the support because of the enhanced SMSI effect, leading to peak broadening and an increase in the reaction cutoff temperature of H_2-TPR over the supported FeNi catalysts, as shown in Fig. 4.

3.5. In situ *IR spectroscopy studies*

To further investigate the surface active species during the DRE reaction, *in situ* IR spectroscopy studies were carried out at temperatures ranging from 373 to 873 K and a total pressure of 2.0 mbar (C_2H_6:CO_2 = 1:1). *In situ* IR spectra of the FeNi/Ce–$Al_{0.1}$, FeNi/Ce–$Al_{0.5}$, and FeNi/Ce–$Al_{0.9}$ catalysts are shown in Figs. S10–S12 in Appendix A. All the spectra were normalized by subtracting the corresponding IR spectrum under vacuum at RT. A typical IR spectrum is divided into three different characteristic vibrational regions that will be discussed individually.

The *in situ* IR spectra in the region of 3900–3500 cm^{-1} in Fig. 8 provide information on surface hydroxyl and carbonate species. The wide band at 3770–3790 cm^{-1} and the strong band at approximately 3706 cm^{-1} are ascribed to the monocoordinated OH groups (Type I OH) of Al and Ce, respectively [65–68]. The band at approximately 3732 cm^{-1} is mainly ascribed to the Type II-A OH species of Al (hydroxyl groups bibridged across Al–Al ion pairs) with a possible contribution of terminal OH groups bound to surface Ce^{4+} cations [65]. The band located at approximately 3625 cm^{-1} is thought to be a combination of two bands: ① the Type II-B OH species of Ce with adjacent oxygen vacancies (O–Ce–OH–Ce–□) at 3630 cm^{-1}; and ② the surface bicarbonate (HCO_3^-) species at 3619 cm^{-1}, as confirmed by the delay of the band at approximately 3706 cm^{-1} [67,68]. The presence of Type II-B OH species and the absence of Type II-A OH species of Ce indicate that the surface of the FeNi/Al–Ce–O catalysts is highly active with oxygen vacancies under the reaction atmosphere. The band at approximately 3598 cm^{-1} can also be separated into two bands: the tribridged OH species (Type III OH) of Ce at approximately 3600 cm^{-1} and surface protonated carboxylate species (–COOH) at approximately 3593 cm^{-1} [67–70]. The formation of surface carbonate species will be discussed in detail below. As seen in Figs. 2(d) and 3(d), as the reaction temperature increases, the decreased intensity of the OH band over the FeNi/Ce–$Al_{0.5}$ catalyst implies a reduction in H_2O production, which further leads to lower RWGS activity and a higher H_2/CO ratio than those of other supported FeNi catalysts.

The bands in the region of 3150–2750 cm^{-1} correspond to the CH stretching bands of adsorbed species. The strong wide bands at approximately 3005 and 2931 cm^{-1} in Fig. 9 can be ascribed to the antisymmetrical (ν_{as}) and symmetric (ν_s) CH stretching

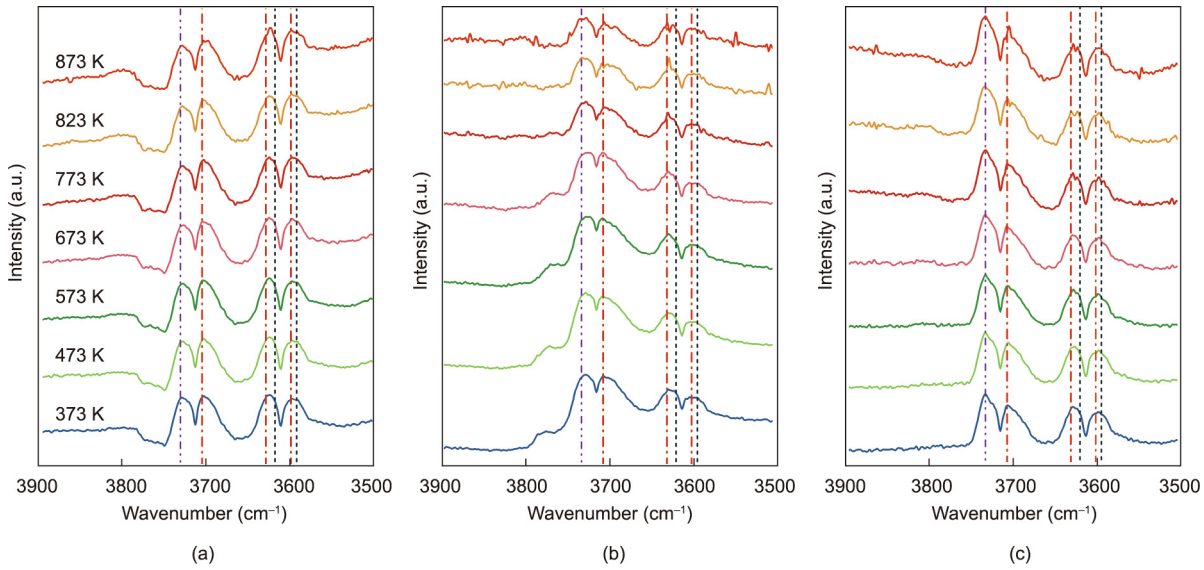

Fig. 8. *In situ* IR spectra of (a) FeNi/Ce–$Al_{0.1}$, (b) FeNi/Ce–$Al_{0.5}$, and (c) FeNi/Ce–$Al_{0.9}$ in the region of 3900–3500 cm^{-1} at temperatures ranging from 373 to 873 K and a total pressure of 2.0 mbar (C_2H_6:CO_2 = 1:1).

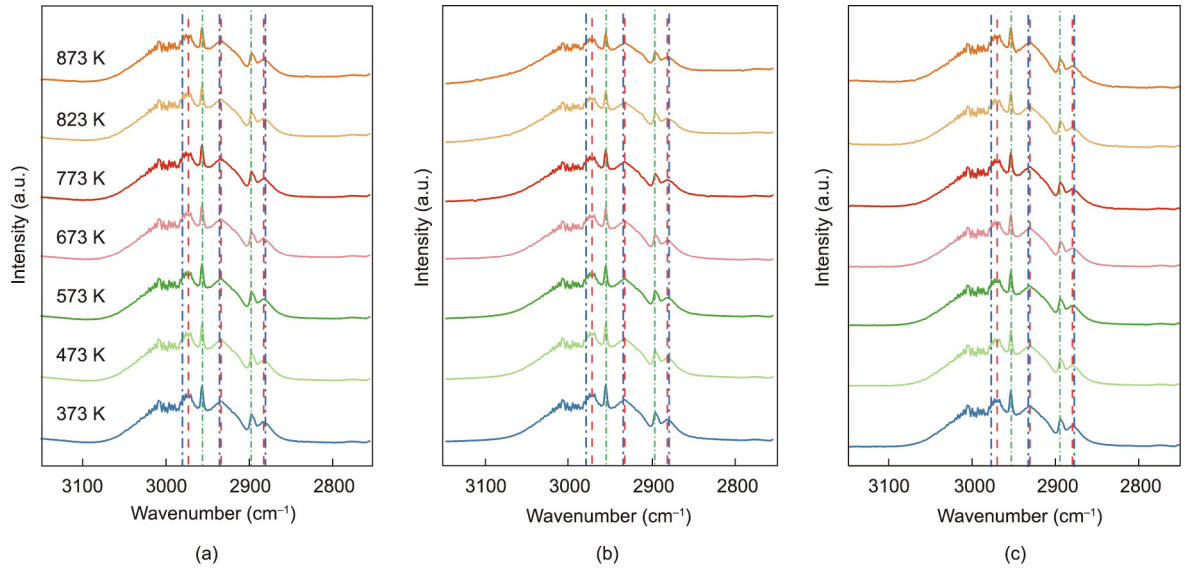

Fig. 9. *In situ* IR spectra of (a) FeNi/Ce–$Al_{0.1}$, (b) FeNi/Ce–$Al_{0.5}$, and (c) FeNi/Ce–$Al_{0.9}$ in the region of 3150–2750 cm^{-1} at temperatures ranging from 373 to 873 K and a total pressure of 2.0 mbar (C_2H_6:CO_2 = 1:1).

vibrations of a series of methyl species in the gas phase [71]. The CH vibration bands in this region indicate the presence of adsorbed ethyl (ν_{as,CH_3} at 2970 cm^{-1}, ν_{as,CH_2} at 2931 cm^{-1}, and ν_{s,CH_3} at 2880 cm^{-1}) [72,73] and ethanol (ν_{as,CH_3} at 2977 cm^{-1}, ν_{as,CH_2} at 2933 cm^{-1}, and ν_{s,CH_3} at 2878 cm^{-1}) [73–75]. The sharp band at 2953 cm^{-1} is ascribed to the CH vibration band of bridged formate species, while the other sharp band at 2895 cm^{-1} is attributed to the CH stretching band of bidentate formate [67,76,77]. Little difference in the spectra of the three catalysts is observed in the temperature range from 373 to 873 K in the region of 3150–2750 cm^{-1}, which means that the FeNi/Al–Ce–O catalysts have the same kind of surface CH-containing species during the reaction, independent of the Al content and reaction temperature.

Fig. S13 in Appendix A shows the *in situ* IR spectra in the region of 1800–1000 cm^{-1}, where the peaks are mainly ascribed to the carbonate-like (OCO) species adsorbed on the samples [67,68,77–79]. The complex band assignments of different carbonate, carboxylate, and formate species adsorbed on the supported FeNi catalysts are summarized in Table S2 in Appendix A. The peaks attributed to the corresponding carbonate-like species are marked in the original spectra of FeNi/Al–Ce–O in Fig. 10. The band distribution in the IR spectra over the FeNi/Ce–$Al_{0.1}$ catalyst in Fig. 10(a) is quite similar to those of the other two samples in Figs. 10(b) and (c), except for the bands at 1430–1425, 1236–1217, and 1057–1050 cm^{-1}. The CO adsorption IR spectra of the FeNi/Ce–$Al_{0.5}$ catalysts are shown in Fig. 10(d) for comparison. The missing bands at 1430–1425 cm^{-1} in both Figs. 10(a) and (d) are attributed to the intermediate adsorbed species of C_2H_6. Since it has been reported that the bands at 1580 cm^{-1} ($\nu_{as,OCO}$), 1429 cm^{-1} ($\nu_{s,OCO}$), 1306 cm^{-1} (δ_{CH_3}), and 1026 cm^{-1} (ρ_{CH_3}) are the characteristic peaks of acetate species, an oxidation product of C_2H_6 on CeO_2 at 355 K [74], the increased IR spectral intensity for the FeNi/Ce–$Al_{0.5}$ and FeNi/Ce–$Al_{0.9}$ catalysts at 1430–1425 cm^{-1} can be attributed to the formation of surface acetate species. The bands at 1660–

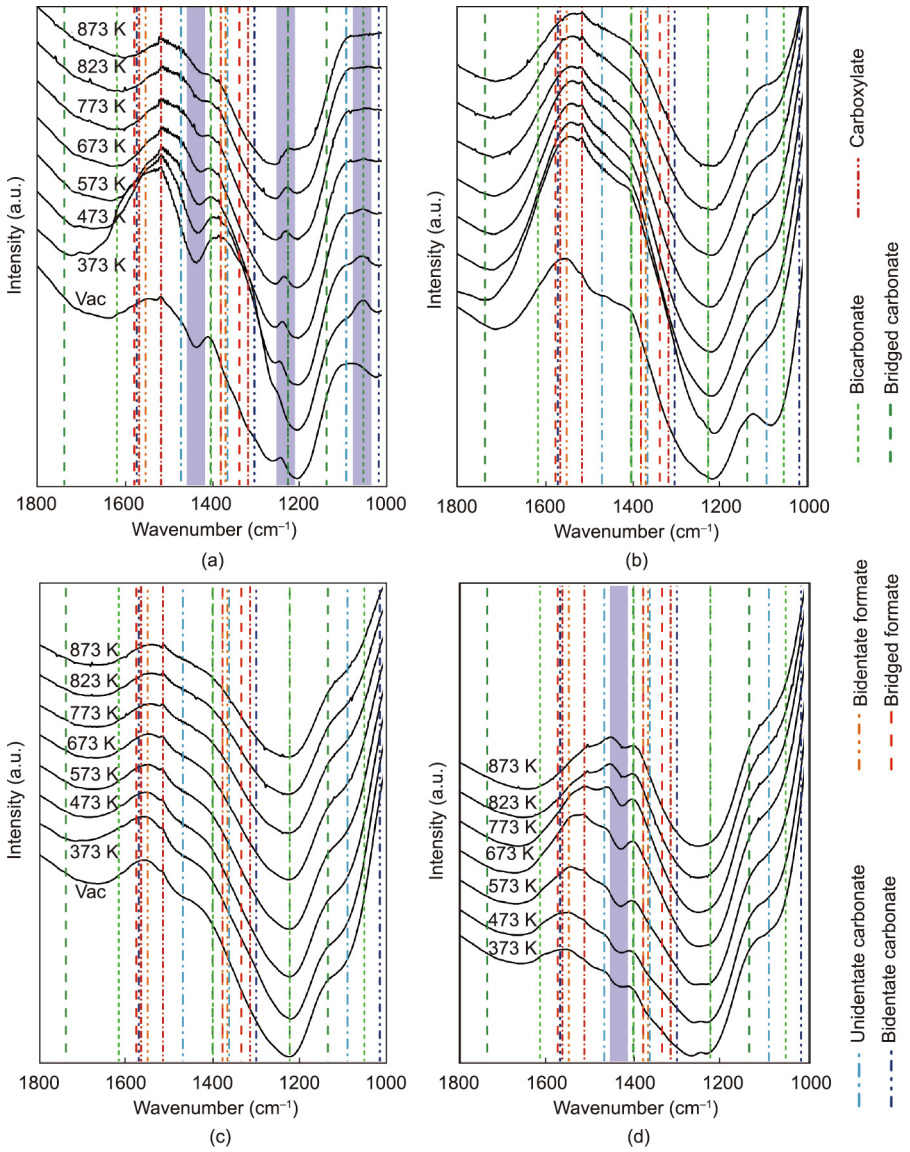

Fig. 10. Original *in situ* IR spectra of (a) FeNi/Ce–$Al_{0.1}$, (b) FeNi/Ce–$Al_{0.5}$, and (c) FeNi/Ce–$Al_{0.9}$ in the region of 1800–1000 cm^{-1} at temperatures ranging from 373 to 873 K and a total pressure of 2.0 mbar (C_2H_6:CO_2 = 1:1). (d) *In situ* IR spectra of CO adsorption over the FeNi/Ce–$Al_{0.5}$ catalyst in the region of 1800–1000 cm^{-1} with 5.0 mbar CO from 373 to 573 K and 1.0 mbar CO from 673 to 873 K. Vac: vacuum.

1640 cm^{-1} and approximately 1230 cm^{-1} arising from the olefinic C=C and CH stretching vibrations imply the formation and adsorption of ethylene on the FeNi/Ce–$Al_{0.1}$ catalyst, rather than surface acetate species [80]. Thus, it can be inferred that the different product selectivity of the FeNi/Al–Ce–O catalysts results from the changes in the surface adsorbed species. Moreover, the bands at 1057–1050 cm^{-1} in Fig. 10(a) below 673 K are attributed to the CO stretching vibration of bidentate ethoxide and methoxide species [74,75]. Since the formation of the $^*C_2H_yO$ intermediate has proven to be essential for C–C bond cleavage and syngas production [7], the reduced band intensity at high reaction temperatures indicates that the weak adsorption of surface bidentate ethoxide species on the FeNi/Ce–$Al_{0.1}$ catalyst is beneficial to the formation of ethylene.

3.6. Reaction mechanism

On the basis of the discussion above, a typical catalytic cycle of CO_2 over FeNi/Al–Ce–O catalysts involves the following process, as shown in Fig. 11. CO_2 in the gas phase first adsorbs onto the surface hydroxyl species or oxygen vacancies and generates adsorbed carbonate-like species, such as bicarbonate and carboxylate. In addition, C_2H_6 adsorbs on metallic or oxidized FeNi active sites and dissociates into ethyl or ethoxy groups and a hydrogen atom. As a result of surface hydrogen spillover, adsorbed bicarbonate or carboxylate species are reduced to carboxylic acid or formate species, which further decompose into surface hydroxyl and carbonyl species through a possible formyl transition intermediate [77]. Surface hydroxyl species or oxygen vacancies regenerate after the release of CO to the gas phase. Nevertheless, the oxidation of C_2H_6 involves two different paths determined by the dispersion of FeNi active components. The impregnation of Fe and Ni precursors on pure CeO_2 tends to generate bimetallic FeNi NPs, which prevents the excessive oxidation of adsorbed ethyl or ethoxy species and improves the selectivity of ethylene [45]. The introduction of Al into the lattice of CeO_2 greatly improves not only the content of surface Ce^{3+} species and oxygen vacancies but also the dispersion of surface active components through the enhanced SMSI

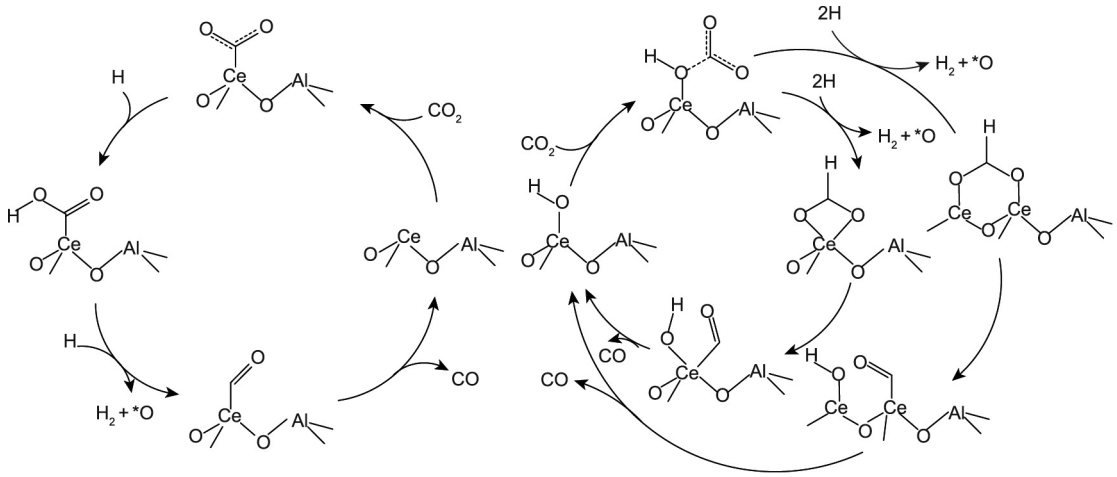

Fig. 11. Typical catalytic cycle of CO_2 over FeNi/Al–Ce–O catalysts.

effect. The strong interaction between FeNi and the Al–Ce–O support stabilizes the adsorbed ethoxy moiety and its further oxidation products, which are essential for C–C bond cleavage and syngas generation.

4. Conclusions

FeNi/Al–Ce–O catalysts synthesized via a facile sol–gel and impregnation method exhibit a composition-induced SMSI effect for DRE. The Al content in the Al–Ce–O supports significantly influences the metal–support interface structure of the catalysts and further determines the catalytic properties during the reaction. As the Al content increases, the C_2H_6 and CO_2 conversion, CO selectivity and yield, and TOF first increase and then decrease according to the same trend as the TESA. The FeNi/Ce–$Al_{0.5}$ catalyst exhibits the best DRE performance with the highest C_2H_6 conversion (11.7%), CO_2 conversion (33.1%), and CO yield (11.5%). The increased surface oxygen vacancy partially inhibits the RWGS reaction over FeNi/Ce–$Al_{0.5}$ catalysts, which leads to a higher H_2/CO ratio than that of other FeNi/Al–Ce–O catalysts. The selectivity over the supported FeNi catalysts is determined by the dispersion of the surface active components. As the Al content in the Al–Ce–O supports increases, the dispersion of surface active components is promoted by the enhanced SMSI effect over the supported FeNi catalysts. The enhanced SMSI effect stabilizes the adsorbed $*C_2H_yO$ intermediate and produces excessive oxidation products, leading to C–C bond cleavage and syngas generation. In summary, the introduction of Al into the CeO_2 support not only increases the content of surface Ce^{3+} and oxygen vacancies but also promotes the dispersion of surface active components, which further adjusts the catalytic properties for DRE over supported FeNi catalysts.

Acknowledgments

The authors gratefully acknowledge the support from the National Key Research and Development Program of China (2017YFB0702800), the China Petrochemical Corporation (Sinopec Group), and the National Natural Science Foundation of China (91434102 and U1663221).

Compliance with ethics guidelines

Tao Zhang, Zhi-Cheng Liu, Ying-Chun Ye, Yu Wang, He-Qin Yang, Huan-Xin Gao, and Wei-Min Yang declare that they have no conflicts of interest or financial conflicts to disclose.

Appendix A. Supplementary data

Supplementary data to this article can be found online at https://doi.org/10.1016/j.eng.2021.11.027.

References

[1] Knutson TR, Tuleya RE. Impact of CO_2-induced warming on simulated hurricane intensity and precipitation: sensitivity to the choice of climate model and convective parameterization. J Clim 2004;17(18):3477–95.
[2] Hansen J, Sato M, Ruedy R, Lo K, Lea DW, Medina-Elizade M. Global temperature change. Proc Natl Acad Sci USA 2006;103(39):14288–93.
[3] Hoegh-Guldberg O, Bruno JF. The impact of climate change on the world's marine ecosystems. Science 2010;328(5985):1523–8.
[4] Mimura N, Takahara I, Inaba M, Okamoto M, Murata K. High-performance Cr/H-ZSM-5 catalysts for oxidative dehydrogenation of ethane to ethylene with CO_2 as an oxidant. Catal Commun 2002;3(6):257–62.
[5] Porosoff MD, Myint MNZ, Kattel S, Xie Z, Gomez E, Liu P, et al. Identifying different types of catalysts for CO_2 reduction by ethane through dry reforming and oxidative dehydrogenation. Angew Chem Int Ed Engl 2015;54(51):15501–5.
[6] Myint MNZ, Yan B, Wan J, Zhao S, Chen JG. Reforming and oxidative dehydrogenation of ethane with CO_2 as a soft oxidant over bimetallic catalysts. J Catal 2016;343:168–77.
[7] Kattel S, Chen JG, Liu P. Mechanistic study of dry reforming of ethane by CO_2 on a bimetallic PtNi(111) model surface. Catal Sci Technol 2018;8(15):3748–58.
[8] Rostrup-Nielsen JR. Production of synthesis gas. Catal Today 1993;18(4):305–24.
[9] Rostrup-Nielsen JR, Christensen TS, Dybkjaer I. Steam reforming of liquid hydrocarbons. Stud Surf Sci Catal 1998;113:81–95.
[10] Bharadwaj SS, Schmidt LD. Catalytic partial oxidation of natural gas to syngas. Fuel Process Technol 1995;42(2–3):109–27.
[11] Wang S, Lu GQ, Millar GJ. Carbon dioxide reforming of methane to produce synthesis gas over metal-supported catalysts: state of the art. Energy Fuels 1996;10(4):896–904.
[12] Liu Z, Zhou J, Cao K, Yang W, Gao H, Wang Y, et al. Highly dispersed nickel loaded on mesoporous silica: one-spot synthesis strategy and high performance as catalysts for methane reforming with carbon dioxide. Appl Catal B Environ 2012;125:324–30.
[13] Wang N, Shen K, Huang L, Yu X, Qian W, Chu W. Facile route for synthesizing ordered mesoporous Ni–Ce–Al oxide materials and their catalytic performance for methane dry reforming to hydrogen and syngas. ACS Catal 2013;3(7):1638–51.
[14] Liu Z, Lustemberg P, Gutiérrez RA, Carey JJ, Palomino RM, Vorokhta M, et al. *In situ* investigation of methane dry reforming on metal/ceria(111) surfaces: metal–support interactions and C–H bond activation at low temperature. Angew Chem Int Ed Engl 2017;56(42):13041–6.
[15] Pakhare D, Spivey J. A review of dry (CO_2) reforming of methane over noble metal catalysts. Chem Soc Rev 2014;43(22):7813–37.
[16] Muraza O, Galadima A. A review on coke management during dry reforming of methane. Int J Energy Res 2015;39(9):1196–216.
[17] Yan B, Yang X, Yao S, Wan J, Myint MNZ, Gomez E, et al. Dry reforming of ethane and butane with CO_2 over PtNi/CeO_2 bimetallic catalysts. ACS Catal 2016;6(11):7283–92.
[18] Therdthianwong S, Therdthianwong A, Siangchin C, Yongprapat S. Synthesis gas production from dry reforming of methane over Ni/Al_2O_3 stabilized by ZrO_2. Int J Hydrogen Energy 2008;33(3):991–9.

[19] Kambolis A, Matralis H, Trovarelli A, Papadopoulou C. Ni/CeO_2–ZrO_2 catalysts for the dry reforming of methane. Appl Catal A Gen 2010;377(1–2):16–26.
[20] Zhang S, Muratsugu S, Ishiguro N, Tada M. Ceria-doped Ni/SBA-16 catalysts for dry reforming of methane. ACS Catal 2013;3(8):1855–64.
[21] Ay H, Üner D. Dry reforming of methane over CeO_2 supported Ni, Co and Ni–Co catalysts. Appl Catal B Environ 2015;179:128–38.
[22] Li X, Li D, Tian H, Zeng L, Zhao ZJ, Gong J. Dry reforming of methane over Ni/La_2O_3 nanorod catalysts with stabilized Ni nanoparticles. Appl Catal B Environ 2017;202:683–94.
[23] Crisafulli C, Scirè S, Maggiore R, Minicò S, Galvagno S. CO_2 reforming of methane over Ni–Ru and Ni–Pd bimetallic catalysts. Catal Lett 1999;59(1):21–6.
[24] San-José-Alonso D, Juan-Juan J, Illán-Gómez MJ, Román-Martínez MC. Ni, Co and bimetallic Ni–Co catalysts for the dry reforming of methane. Appl Catal A Gen 2009;371(1–2):54–9.
[25] García-Diéguez M, Finocchio E, Larrubia MÁ, Alemany LJ, Busca G. Characterization of alumina-supported Pt, Ni and PtNi alloy catalysts for the dry reforming of methane. J Catal 2010;274(1):11–20.
[26] Wen S, Liang M, Zou J, Wang S, Zhu X, Liu Li, et al. Synthesis of a SiO_2 nanofibre confined Ni catalyst by electrospinning for the CO_2 reforming of methane. J Mater Chem A 2015;3(25):13299–307.
[27] Guo Y, Zou J, Shi X, Rukundo P, Wang Z. A Ni/CeO_2–CDC-SiC catalyst with improved coke resistance in CO_2 reforming of methane. ACS Sustain Chem Eng 2017;5(3):2330–8.
[28] Guo Y, Li Y, Ning Y, Liu Q, Tian L, Zhang R, et al. CO_2 Reforming of methane over a highly dispersed Ni/Mg–Al–O catalyst prepared by a facile and green method. Ind Eng Chem Res 2020;59(35):15506–14.
[29] Juan-Juan J, Román-Martínez MC, Illán-Gómez MJ. Effect of potassium content in the activity of K-promoted Ni/Al_2O_3 catalysts for the dry reforming of methane. Appl Catal A Gen 2006;301(1):9–15.
[30] Pechimuthu NA, Pant KK, Dhingra SC. Deactivation studies over Ni−K/CeO_2−Al_2O_3 catalyst for dry reforming of methane. Ind Eng Chem Res 2007;46(6):1731–6.
[31] Rezaei M, Alavi SM, Sahebdelfar S, Yan ZF. Effects of K_2O promoter on the activity and stability of nickel catalysts supported on mesoporous nanocrystalline zirconia in CH_4 reforming with CO_2. Energy Fuels 2008;22(4):2195–202.
[32] Rodriguez G, Bedel L, Roger AC, Udron L, Carballo L, Kiennemann A. Dry reforming of ethane on trimetallic perovskites $LaCo_xFe_{1-x}O_3$: characterizations and reactivity. In: Liu CJ, Mallinson RG, Aresta M, editors. Utilization of greenhouse gases. Washington, DC: American Chemical Society; 2003. p. 69–82.
[33] Zhao B, Yan B, Yao S, Xie Z, Wu Q, Ran R, et al. $LaFe_{0.9}Ni_{0.1}O_3$ perovskite catalyst with enhanced activity and coke-resistance for dry reforming of ethane. J Catal 2018;358:168–78.
[34] Liu Y, Wu Y, Akhtamberdinova Z, Chen X, Jiang G, Liu D. Dry reforming of shale gas and carbon dioxide with Ni–Ce–Al_2O_3 catalyst: syngas production enhanced over Ni–CeO_x formation. ChemCatChem 2018;10(20):4689–98.
[35] Al-Mamoori A, Rownaghi AA, Rezaei F. Combined capture and utilization of CO_2 for syngas production over dual-function materials. ACS Sustain Chem Eng 2018;6(10):13551–61.
[36] Du X, Zhang D, Shi L, Gao R, Zhang J. Morphology dependence of catalytic properties of Ni/CeO_2 nanostructures for carbon dioxide reforming of methane. J Phys Chem C 2012;116(18):10009–16.
[37] Wang N, Qian W, Chu W, Wei F. Crystal-plane effect of nanoscale CeO_2 on the catalytic performance of Ni/CeO_2 catalysts for methane dry reforming. Catal Sci Technol 2016;6(10):3594–605.
[38] Liu Z, Grinter DC, Lustemberg PG, Nguyen-Phan TD, Zhou Y, Luo S, et al. Dry reforming of methane on a highly-active Ni–CeO_2 catalyst: effects of metal–support interactions on C–H bond breaking. Angew Chem Int Ed Engl 2016;55(26):7455–9.
[39] Lustemberg PG, Ramírez PJ, Liu Z, Gutiérrez RA, Grinter DG, Carrasco J, et al. Room-temperature activation of methane and dry re-forming with CO_2 on Ni–CeO_2(111) surfaces: effect of Ce^{3+} sites and metal–support interactions on C–H bond cleavage. ACS Catal 2016;6(12):8184–91.
[40] Xie Z, Yan B, Lee JH, Wu Q, Li X, Zhao B, et al. Effects of oxide supports on the CO_2 reforming of ethane over Pt–Ni bimetallic catalysts. Appl Catal B Environ 2019;245:376–88.
[41] Wang N, Xu Z, Deng J, Shen K, Yu X, Qian W, et al. One-pot synthesis of ordered mesoporous NiCeAl oxide catalysts and a study of their performance in methane dry reforming. ChemCatChem 2014;6(5):1470–80.
[42] Gao Q, Hao J, Qiu Y, Hu S, Hu Z. Electronic and geometric factors affecting oxygen vacancy formation on CeO_2(111) surfaces: a first-principles study from trivalent metal doping cases. Appl Surf Sci 2019;497:143732.
[43] Yang L, Pastor-Pérez L, Gu S, Sepúlveda-Escribano A, Reina TR. Highly efficient Ni/CeO_2–Al_2O_3 catalysts for CO_2 upgrading via reverse water–gas shift: effect of selected transition metal promoters. Appl Catal B Environ 2018;232:464–71.
[44] Kim SM, Abdala PM, Margossian T, Hosseini D, Foppa L, Armutlulu A, et al. Cooperativity and dynamics increase the performance of NiFe dry reforming catalysts. J Am Chem Soc 2017;139(5):1937–49.
[45] Yan B, Yao S, Kattel S, Wu Q, Xie Z, Gomez E, et al. Active sites for tandem reactions of CO_2 reduction and ethane dehydrogenation. Proc Natl Acad Sci USA 2018;115(33):8278–83.
[46] Morris SM, Fulvio PF, Jaroniec M. Ordered mesoporous alumina-supported metal oxides. J Am Chem Soc 2008;130(45):15210–6.
[47] Yuan Q, Duan HH, Li LL, Li ZX, Duan WT, Zhang LS, et al. Homogeneously dispersed ceria nanocatalyst stabilized with ordered mesoporous alumina. Adv Mater 2010;22(13):1475–8.
[48] Li ZX, Shi FB, Zhang T, Wu HS, Sun LD, Yan CH. Ytterbium stabilized ordered mesoporous titania for near-infrared photocatalysis. Chem Commun 2011;47(28):8109–11.
[49] Sun J, Feng Q, Liu Q, Ji S, Fang Y, Peng X, et al. An Al_2O_3-coated SiC-supported Ni catalyst with enhanced activity and improved stability for production of synthetic natural gas. Ind Eng Chem Res 2018;57(44):14899–909.
[50] Rose AJ. Théorie et technique de la radiocristallographie, par A. Guinier. Bull Min 1956;79(10):619–21. French.
[51] de Keijser TH, Langford JI, Mittemeijer EJ, Vogels ABP. Use of the Voigt function in a single-line method for the analysis of X-ray diffraction line broadening. J Appl Cryst 1982;15(3):308–14.
[52] Rai R, Triloki T, Singh BK. X-ray diffraction line profile analysis of KBr thin films. Appl Phys A 2016;122(8):774.
[53] Sasikala R, Sudarsan V, Kulshreshtha SK. ^{27}Al NMR studies of Ce–Al mixed oxides: origin of 40 ppm peak. J Solid State Chem 2002;169(1):113–7.
[54] Romeo M, Bak K, El Fallah J, Le Normand F, Hilaire L. XPS study of the reduction of cerium dioxide. Surf Interface Anal 1993;20(6):508–12.
[55] Pfau A, Schierbaum KD. The electronic structure of stoichiometric and reduced CeO_2 surfaces: an XPS, UPS and HREELS study. Surf Sci 1994;321(1–2):71–80.
[56] Shyu JZ, Weber WH, Gandhi HS. Surface characterization of alumina-supported ceria. J Phys Chem 1988;92(17):4964–70.
[57] Moulder JF, Stickle WF, Sobol PE, Bomben KD. Handbook of X-ray photoelectron spectroscopy. Chastain J, editor. Eden Prairie: Physical Electronics, Inc.; 1992.
[58] Wang WW, Yu WZ, Du PP, Xu H, Jin Z, Si R, et al. Crystal plane effect of ceria on supported copper oxide cluster catalyst for CO oxidation: importance of metal–support interaction. ACS Catal 2017;7(2):1313–29.
[59] Taniguchi T, Watanabe T, Sugiyama N, Subramani AK, Wagata H, Matsushita N, et al. Identifying defects in ceria-based nanocrystals by UV resonance Raman spectroscopy. J Phys Chem C 2009;113(46):19789–93.
[60] Wu Z, Li M, Howe J, Meyer 3rd HM, Overbury SH. Probing defect sites on CeO_2 nanocrystals with well-defined surface planes by Raman spectroscopy and O_2 adsorption. Langmuir 2010;26(21):16595–606.
[61] He D, Chen D, Hao H, Yu J, Liu J, Lu J, et al. Structural/surface characterization and catalytic evaluation of rare-earth (Y, Sm and La) doped ceria composite oxides for CH_3SH catalytic decomposition. Appl Surf Sci 2016;390:959–67.
[62] Chen D, He D, Lu J, Zhong L, Liu F, Liu J, et al. Investigation of the role of surface lattice oxygen and bulk lattice oxygen migration of cerium-based oxygen carriers: XPS and designed H_2-TPR characterization. Appl Catal B Environ 2017;218:249–59.
[63] Mierczynski P, Mierczynska A, Ciesielski R, Mosinska M, Nowosielska M, Czylkowska A, et al. High active and selective Ni/CeO_2–Al_2O_3 and Pd–Ni/CeO_2–Al_2O_3 catalysts for oxy-steam reforming of methanol. Catalysts 2018;8(9):380.
[64] Karim W, Spreafico C, Kleibert A, Gobrecht J, VandeVondele J, Ekinci Y, et al. Catalyst support effects on hydrogen spillover. Nature 2017;541(7635):68–71.
[65] Morterra C, Bolis V, Magnacca G. Surface characterization of modified aluminas. Part 4.—Surface hydration and Lewis acidity of CeO_2–Al_2O_3 systems. J Chem Soc Faraday Trans 1996;92(11):1991–9.
[66] Zaki MI, Hasan MA, Al-Sagheer FA, Pasupulety L. *In situ* FTIR spectra of pyridine adsorbed on SiO_2–Al_2O_3, TiO_2, ZrO_2 and CeO_2: general considerations for the identification of acid sites on surfaces of finely divided metal oxides. Colloids Surf A Physicochem Eng Asp 2001;190(3):261–74.
[67] Pozdnyakova O, Teschner D, Wootsch A, Krohnert J, Steinhauer B, Sauer H, et al. Preferential CO oxidation in hydrogen (PROX) on ceria-supported catalysts, part I: oxidation state and surface species on Pt/CeO_2 under reaction conditions. J Catal 2006;237(1):1–16.
[68] Pozdnyakova O, Teschner D, Wootsch A, Krohnert J, Steinhauer B, Sauer H, et al. Preferential CO oxidation in hydrogen (PROX) on ceria-supported catalysts, part II: oxidation states and surface species on Pd/CeO_2 under reaction conditions, suggested reaction mechanism. J Catal 2006;237(1):17–28.
[69] Badri A, Binet C, Lavalley JC. An FTIR study of surface ceria hydroxy groups during a redox process with H_2. J Chem Soc Faraday Trans 1996;92(23):4669–73.
[70] Binet C, Daturi M, Lavalley JC. IR study of polycrystalline ceria properties in oxidised and reduced states. Catal Today 1999;50(2):207–25.
[71] Raskó J, Kiss J. Adsorption and surface reactions of acetaldehyde on TiO_2, CeO_2 and Al_2O_3. Appl Catal A Gen 2005;287(2):252–60.
[72] Trautmann S, Baerns M, Auroux A. *In situ* infrared spectroscopic and catalytic studies on the oxidation of ethane over supported palladium catalysts. J Catal 1992;136(2):613–6.
[73] Zhang R, Wang H, Tang S, Liu C, Dong F, Yue H, et al. Photocatalytic oxidative dehydrogenation of ethane using CO_2 as a soft oxidant over Pd/TiO_2 catalysts to C_2H_4 and syngas. ACS Catal 2018;8(10):9280–6.
[74] Yee A, Morrison SJ, Idriss H. A study of the reactions of ethanol on CeO_2 and Pd/CeO_2 by steady state reactions, temperature programmed desorption, and *in situ* FT-IR. J Catal 1999;186(2):279–95.
[75] Yee A, Morrison SJ, Idriss H. A study of ethanol reactions over Pt/CeO_2 by temperature-programmed desorption and *in situ* FT-IR spectroscopy: evidence of benzene formation. J Catal 2000;191(1):30–45.
[76] Hwang K, Ihm S, Park J. Enhanced CeO_2-supported Pt catalyst for water–gas shift reaction. Fuel Process Technol 2010;91(7):729–36.

[77] Li C, Sakata Y, Arai T, Domen K, Maruya K, Onishi T. Adsorption of carbon monoxide and carbon dioxide on cerium oxide studied by Fourier-transform infrared spectroscopy. Part 2.—Formation of formate species on partially reduced CeO_2 at room temperature. J Chem Soc Faraday Trans 1 1989;85(6):1451–61.
[78] Li C, Sakata Y, Arai T, Domen K, Maruya K, Onishi T. Carbon monoxide and carbon dioxide adsorption on cerium oxide studied by Fourier-transform infrared spectroscopy. Part 1.—Formation of carbonate species on dehydroxylated CeO_2, at room temperature. J Chem Soc Faraday Trans 1 1989;85(4):929–43.
[79] Saw ET, Oemar U, Tan XR, Du Y, Borgna A, Hidajat K, et al. Bimetallic Ni–Cu catalyst supported on CeO_2 for high-temperature water–gas shift reaction: methane suppression via enhanced CO adsorption. J Catal 2014;314:32–46.
[80] Heracleous E, Lemonidou AA, Lercher JA. Mechanistic features of the ethane oxidative dehydrogenation by *in situ* FTIR spectroscopy over a MoO_3/Al_2O_3 catalyst. Appl Catal A Gen 2004;264(1):73–80.